Determining Titan's Spin State from Cassini RADAR Images

Bryan W. Stiles[1], Randolph L. Kirk[2], Ralph D. Lorenz[3], Scott Hensley[1], Ella Lee[2], Steven J. Ostro[1], Michael D. Allison[4], Philip S. Callahan[1],Yonggyu Gim[1], Luciano Iess[5], Paolo Perci del Marmo[5], Gary Hamilton[1], William T.K. Johnson[1], Richard D. West[1] and the Cassini RADAR Team

Author affiliations and addresses:
1 Jet Propulsion Laboratory, California Institute of Technology,
  4800 Oak Grove Dr Pasadena CA 91109;
2 United States Geological Survey,
  2255 N. Gemini Dr. Flagstaff AZ 86001;
3 Applied Physics Laboratory, Johns Hopkins University,
  11100 Johns Hopkins Road, Laurel MD 20723;
4 NASA Goddard Institute for Space Studies,
  2880 Broadway, New York, NY 10025;
5 University of Rome, Department of Aerospace Engineering and Astronautics,
  via Eudossiana 18, Rome, Italy

Abstract: For some 19 areas of Titan's surface, the Cassini RADAR instrument has obtained SAR images during two different flybys. The time interval between flybys varies from several weeks to two years. We have used the apparent misregistration (by 10-30 km) of features between separate flybys to construct a refined model of Titan's spin state, estimating six parameters: North pole right ascension and declination, spin rate, and these quantities' first time derivatives We determine a pole location with right ascension of 39.48 degrees and declination of 83.43 degrees corresponding to a 0.3-degree obliquity. We determine the spin rate to be 22.5781 deg/day or 0.001 degrees per day faster than the synchronous spin rate. Our estimated corrections to the pole and spin rate exceed their corresponding standard errors by factors of 80 and 8, respectively. We also found that the rate of change in the pole right ascension is -30 deg/century, ten times faster than right ascension rate of change for the orbit normal. The spin rate is increasing at a rate of 0.05 deg/day per century. We observed no significant change in pole declination over the period for which we have data. Applying our pole correction reduces the feature misregistration from tens of km to 3 km. Applying the spin rate and derivative corrections further reduces the misregistration to 1.2 km.[1]*
Subject Headings: Solar System, Astronomical Instrumentation Methods and Techniques

1 Introduction

The Cassini RADAR instrument is a 13.8 GHz burst-mode radar. In Synthetic Aperture Radar (SAR) mode it maps ~2000 km long by ~200 km wide strips of Titan's surface with a resolution of 300 m to 1 km depending upon the position within the strip. So far, Cassini RADAR has obtained 14 such strips during Titan flybys. Occasionally, multiple strips overlap. By co-registering identical features within overlaps, we can determine how the surface of Titan has moved between observations and thus estimate Titan's pole location and spin rate. Similar work was also performed using SAR imagery from Magellan to estimate the spin model of Venus (Davies et al. 1992).

Our estimation technique is a three-step procedure. First, we select a set of recognizable landmarks that have each been observed in two different SAR images obtained at different times. Second, we locate the landmarks in the inertial frame using the Doppler frequency and range of each landmark, and the spacecraft's inertial frame position and velocity vectors. Finally, we estimate the spin state parameters by minimizing the misregistration error, that is, the apparent movement in Titan body fixed coordinates of the landmarks between observation times. The details of the technique and potential sources of error are discussed in the next section. The dominant source of error is landmark mismatching, which results in random co-registration errors with approximately 1 km standard deviation per spatial component. This error is much smaller than the co-registration error we obtain using the nominal International Astronomical Union (IAU) Titan spin model (Davies et al. 1989, Jacobson et al. 2004) which is tens of km in magnitude. The inaccuracy in the IAU model is not surprising. In the absence of data, it was developed by assuming zero obliquity. Utilizing Cassini SAR data, we are able to measure the location of the spin axis precisely and determine that the spin rate is significantly asynchronous. We describe details of the technique and potential sources of error in the next three sections.

---

2 Step I: Landmark Selection

The first step in our spin state estimation is landmark selection. Each landmark L_k used in our estimation must have been observed in two of the 14 SAR images that have been obtained by Cassini RADAR. The interval between the acquisition times of the two images varies from several weeks to two years. For convenience, if a landmark has been observed in three images, it is treated as if it were three separate twice-observed landmarks. Only a handful of landmarks have been observed three times and none have been observed more than three times. We select each landmark manually by examining regions in which the SAR images overlap. When a landmark is selected, we choose a pixel in each SAR image that corresponds as closely as possible to the same point on the landmark. When selection is complete we have N landmarks L_k, for k =1,2,3,…,N. Two sets of landmarks were identified, a set of N=50 from 10 SAR image overlap pairs and a set of N=151 from 17 overlap pairs. The 50-landmark set was chosen first, then an additional 101 landmarks of somewhat lesser quality were determined. The parameters determined from the two sets were nearly identical but the N=151 set had a significantly larger residual error after the fit. This is to be expected because the final 100 landmarks were chosen after the best candidates had already been selected. Unless otherwise mentioned, the results discussed in this paper are for the N=50 set. For each landmark we determine 6 quantities $(t_{k1}, t_{k2}, i_{k1}, i_{k2}, j_{k1}, j_{k2})$, where i_{k1} is the along track pixel index of L_k in the SAR image obtained at time t_{k1}, j_{k1} is the cross track pixel index of L_k in the same image, etc. (More precisely t_{k1} is the time that L_k itself was observed in the earliest acquired SAR image. An entire SAR image is acquired over a 30-40 minute interval, but no individual landmark is observed for more than 40 seconds at a time.) As mentioned previously, the landmark mismatches are the dominant source of error in the technique. A landmark mismatch occurs when (i_{k1}, j_{k1}) and (i_{k2}, j_{k2}) do not correspond to exactly the same position relative to L_k.

Several criteria are used in the selection procedure to minimize landmark mismatches. First, the landmark must be a small, high-contrast feature. Second, it must look sufficiently similar in both images so that we can discount the possibility of high topographic relief over a large number of pixels. Terrain can look very different in SAR images obtained from different look directions. In the extreme case, when a region is viewed from opposite sides one can even obtain an inverse correlation in which the same feature appears darker than its surroundings in one image and brighter in the other. We selected features without the alternating bright and dark edges that are characteristic of large topographic relief. Third, we excluded SAR image artifacts, such as beam boundaries, Doppler scalloping, and speckle noise. Fourth, we excluded periodic terrain such as dune fields in which the chances of mismatches are increased. Exceptions were made for small regions within dune fields with unique identifying features. We utilized a manual landmark selection in order to take advantage of the superior capability of human vision to perform the abstract pattern recognition tasks required to meet these criteria.

Figure 1 depicts one of the 151 landmarks selected. A line of length 10 km is included to show scale. The position of the landmark is offset by 3.5 km in the vertical dimension to illustrate the tolerance to which the human eye can match up landmarks. Most people can readily see the 3.5 km shift. The landmark depicted here is not a best-case scenario, but rather a typical one in which

the SAR viewing geometry varies between passes. Specifically, the intrinsic resolution of the images differs by a factor of 3. Such resolution differences can be a problem for automatic feature matching algorithms but are well handled by human vision.
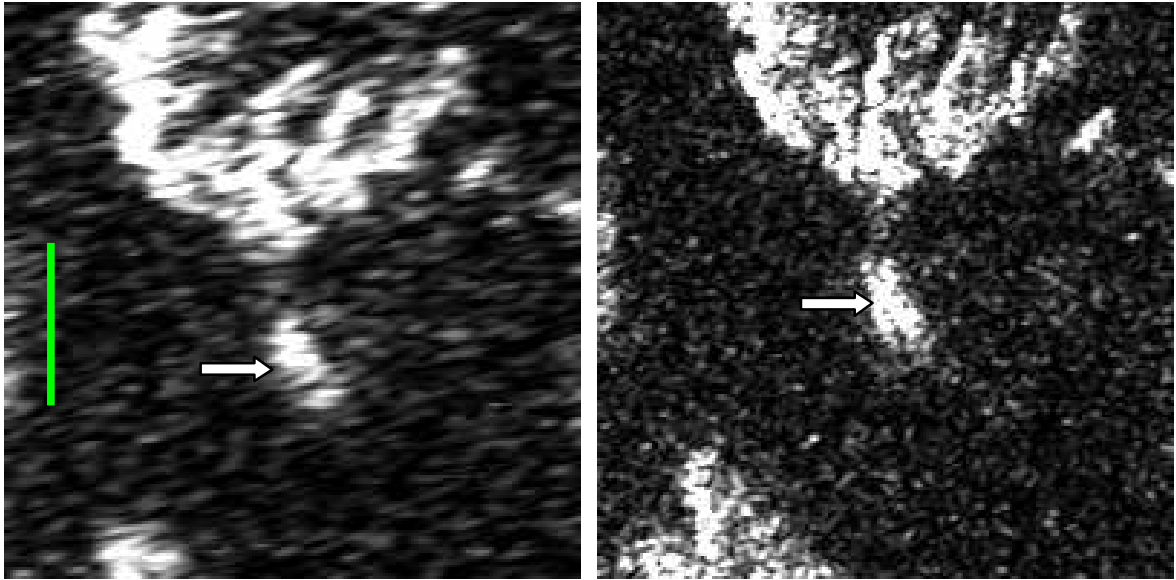

Figure 1: Example of a Landmark: The panel on the left is from Titan flyby T25. The panel on the right is from flyby T28. An arrow indicates the landmark. The green line is 10 km long. Using the zero obliquity IAU Titan spin model, landmarks could be misplaced between images by more than 30 km. Using the spin model reported here, the misplacement distances are reduced to 1-2 km. The figure depicts a 3.5 km vertical shift in landmark location between panels in order to illustrate the ease with which the human eye can detect km scale misregistration.

3 Step II: Landmark Location in Inertial Frame

Once we obtain a set of features, we locate each landmark observation in Titan-centered inertial, non-rotating (J2000) coordinates. (The inertial position of the landmark varies with time due to the rotation of Titan.) First, we determine the Doppler shift and range to target, which are directly measured during SAR image processing. Each pixel in a SAR image is computed from the returned signal energy within a small 2-D interval in Doppler, f_{dop}, and range, r. Secondly, we obtain the spacecraft position, $\mathbf{X}$, and velocity, $\mathbf{V}$, in the inertial frame at each time the landmark was imaged, using spacecraft ephemeris provided by the Cassini Navigation Team. We then transform $\mathbf{X}$ and $\mathbf{V}$ into the nominal IAU Titan rotating frame yielding $\mathbf{X}'$ and $\mathbf{V}'$. The final piece of information, the distance between the landmark and the center of Titan, h, is obtained using a method of estimating topography from SAR (Stiles et al 2007a, 2007b) rather than using Titan's nominal radius. The one-sigma errors bars on this estimate are ±200 m. Using the topography from SAR only slightly impacted the pole location and spin rate parameters but it significantly affected the rate of change in the pole location. When a spherical Titan was assumed, latitude-dependent error in surface height resulted in a -2.0 deg/century solution for the rate of change of pole declination and a 2 km residual mislocation error. When the topography from SAR heights was

4

employed, the rate of change in pole declination reduced to point at which it was indistinguishable from zero and the residual error reduced to 1 km. With Doppler, range, spacecraft ephemeris, and surface height known, we locate the landmark observation by finding the point $\mathbf{P'}$ of intersection among three surfaces: 1) a sphere with radius r centered on $\mathbf{X'}$; 2) a sphere with radius h centered on Titan's center of gravity (0,0,0); and 3) a cone whose apex is at $\mathbf{X'}$ and generating axis is along $\mathbf{V'}$. The angle between the axis of the cone and its surface is given by $\cos^{-1}(f_{dop}\lambda/|2V'|)$. The intersection of the three surfaces, $\mathbf{P'}$, is then transformed back into the inertial coordinate vector $\mathbf{P}$. Due to the coupling between Doppler and spin rate, the errors in the presumed Titan spin model lead to small errors in $\mathbf{P}$. However, the change in Doppler due to refinements in spin model is small, yielding insignificant (~1 m) errors. Errors in spacecraft ephemeris (< 100 m) are a more significant issue, but still small compared to landmark mismatch error. As mentioned in the previous section we utilize two time values for each landmark, the times at which it was observed in each of two Cassini flybys. The method for determining these times and why the durations of each observation are not needed is described in Appendix section A.1. The time, Doppler, range, estimated surface height, spacecraft ephemeris, and carrier wavelength associated with each landmark observation is included in section A.2 to allow a reader to reproduce our analysis.

4 Step III: Spin Parameter Regression

For the final step of the procedure, we solve for the spin model parameter values that minimize co-registration error. We use an iterative gradient-descent method with a momentum term in order to avoid converging on local minima. For each time, the transformation from the non-rotating frame to the rotating/body-fixed frame can be represented by three Euler angles α, β, and θ.

$$\beta = 90 + \phi + \acute{\phi}T; \quad \alpha = 90 - \mu - \acute{\mu}T; \quad \theta = \theta_0 + \omega d + \frac{\acute{\omega}Td}{2} \tag{4.1}$$

Here T is the time in Julian centuries and d in days since 19:16:25 UTC Aug 1, 2006, a time midway through our observed data. The model parameters ϕ, μ, ω, are pole right ascension, pole declination, and spin rate, respectively, at time T=0, and $\acute{\phi}, \acute{\mu}, \acute{\omega}$ are the derivatives of those quantities. The Euler angles β, α, and θ, are applied as follows when transforming from J2000 to Titan body fixed coordinates. The first rotation is β degrees about the z-axis to align the pole with the prime meridian. The second rotation is α degrees about the once-rotated x-axis to align the pole with the z-axis. The third rotation is θ degrees about the twice-rotated z-axis to achieve the correct rotational phase with respect to θ_0, the location of the prime meridian at T=0. The value of θ_0 is an arbitrary choice. To minimize the effect of coordinate system refinements on longitude, we have assigned θ_0 to be the IAU Titan value at T=0. The IAU Titan Euler angles are given by

$$\beta_{IAU} = 90 + 36.41 - 0.036T_0 + 2.66\sin S; \quad \alpha_{IAU} = 90 - 83.94 + 0.004T_0 + 0.30\cos S;$$
$$\theta_{IAU} = 189.64 + 22.5769768\,d_0 - 2.64\sin S; \quad S = 29.80 - 52.1T_0 \tag{4.2}$$

Here, T_0 is the time in Julian centuries and d_0 is in days since J2000.0 (12:00:00 TT Jan. 1, 2000), and S is in degrees. For a given time, the coordinate transformation expressed by Euler angles in (4.1) can be represented by a 3 x 3 rotation matrix. Each of the elements of this matrix is a simple trigonometric function of the Euler angles. Let $\mathbf{A}=[\phi,\mu,\omega,\acute{\phi},\acute{\mu},\acute{\omega}]^T$ be the vector of spin model coordinates. For each landmark L_k, the transformation from J2000 to Titan body fixed coordinates obtained from spin parameter vector $\mathbf{A}$ is represented by rotation matrices $\mathbf{M}_{k1}(\mathbf{A})$ and $\mathbf{M}_{k2}(\mathbf{A})$ at the two observation times t_{k1} and t_{k2}, respectively. The misregistration error for each landmark is the apparent change in its Titan body fixed position from one observation to the next. We minimize the sum of squares of the misregistration errors. The quantity thus minimized is:

$$E_{tot} = \sum_{k=1}^{N}\left(\left\|\mathbf{M}_{k2}(\mathbf{A})\mathbf{P}_{k2} - \mathbf{M}_{k1}(\mathbf{A})\mathbf{P}_{k1}\right\|\right)^2 = \sum_{k=1}^{N}\left(\left\|\mathbf{E}_k\right\|\right)^2 = \sum_{k=1}^{N}\left(P'_{k2x} - P'_{k1x}\right)^2 + \left(P'_{k2y} - P'_{k1y}\right)^2 + \left(P'_{k2z} - P'_{k1z}\right)^2$$

(4.3)

Here $\mathbf{P}_{k1}=[P_{k1x},P_{k1y},P_{k1z}]$ is the 3-D position vector in J2000 of the kth landmark when it was first observed, and $\mathbf{P}_{k2}$ is the J2000 position vector of the landmark during its second observation. $\mathbf{P'}_{k1}$ and $\mathbf{P'}_{k2}$ are the same positions in Titan body fixed coordinates. Although time dependence is not shown explicitly for ease of notation, it should be clear that any vector or matrix with subscript k1 or k2 is valid at time t_{k1}, or t_{k2}, respectively. The minimization problem is solved by finding $\mathbf{A}$, such that $\partial E_{tot}/\partial\mathbf{A}=0$. By utilizing a first order Taylor approximation of $\mathbf{M}$, the problem may be formulated as a linear least squares fit. Let $\mathbf{A}^0$ denote the vector of parameters for the nominal IAU Titan spin model. Let $\mathbf{P}_1$ denote the 3N by 1 column vector formed by concatenating the N non-rotating position vectors $\{\mathbf{P}_{k1}, k=1,2,...N\}$. Let $\mathbf{P}_2$ (size 3N x 1), $\mathbf{E}$ (size 3N by 1), $\mathbf{M}_1$ (size 3N x 6) , and $\mathbf{M}_2$ (size 3N x 6) denote matrices formed in the same manner from the $\{\mathbf{P}_{2k}\}$, $\{\mathbf{E}_k\}$,$\{\mathbf{M}_{1k}\}$, and $\{\mathbf{M}_{2k}\}$ matrices, respectively. Let $\Delta\mathbf{A} = \mathbf{A} - \mathbf{A}^0,\quad \Delta\mathbf{M} = \mathbf{M_2} - \mathbf{M_1},\quad \Delta\mathbf{P} = \mathbf{P_2} - \mathbf{P_1},$ and $\Delta\mathbf{P'} = \mathbf{P'_2} - \mathbf{P'_1} = \mathbf{M_2}\left(\mathbf{A}^0\right)\mathbf{P_2} - \mathbf{M_1}\left(\mathbf{A}^0\right)\mathbf{P_1}$.

The Taylor approximation about $\mathbf{A}=\mathbf{A}^0$ yields:

$$\Delta\mathbf{P'} \approx \Delta\mathbf{P}\left(\frac{\partial(\Delta\mathbf{M})}{\partial\mathbf{A}}\bigg|\mathbf{A} = \mathbf{A_0}\right)\Delta\mathbf{A} = \mathbf{B}\Delta\mathbf{A}$$
(4.4)

$\mathbf{B}$ is a 3N x 6 matrix of the derivatives $\partial\mathbf{E}/\partial\mathbf{A}$ evaluated at $\mathbf{A}=\mathbf{A}^0$. B is given by

$$\mathbf{B} = \begin{vmatrix} \dfrac{\partial E_{1x}}{\partial \phi} & \dfrac{\partial E_{1x}}{\partial \mu} & \dfrac{\partial E_{1x}}{\partial \omega} & \dfrac{\partial E_{1x}}{\partial \acute{\phi}} & \dfrac{\partial E_{1x}}{\partial \acute{\mu}} & \dfrac{\partial E_{1x}}{\partial \acute{\omega}} \\ \dfrac{\partial E_{1y}}{\partial \phi} & \dfrac{\partial E_{1y}}{\partial \mu} & ... & ... & ... & \dfrac{\partial E_{1y}}{\partial \acute{\omega}} \\ \dfrac{\partial E_{1z}}{\partial \phi} & \dfrac{\partial E_{1z}}{\partial \mu} & ... & ... & ... & \dfrac{\partial E_{1z}}{\partial \acute{\omega}} \\ ... & ... & ... & ... & ... & ... \\ \dfrac{\partial E_{Nx}}{\partial \phi} & \dfrac{\partial E_{Nx}}{\partial \mu} & ... & ... & ... & \dfrac{\partial E_{Nx}}{\partial \acute{\omega}} \\ \dfrac{\partial E_{Ny}}{\partial \phi} & \dfrac{\partial E_{Ny}}{\partial \mu} & ... & ... & ... & \dfrac{\partial E_{Ny}}{\partial \acute{\omega}} \\ \dfrac{\partial E_{Nz}}{\partial \phi} & \dfrac{\partial E_{Nz}}{\partial \mu} & ... & ... & ... & \dfrac{\partial E_{Nz}}{\partial \acute{\omega}} \end{vmatrix} \tag{4.5}$$

Finding the $\mathbf{A}$ that minimizes E_{tot} is equivalent to finding the $\Delta\mathbf{A}$ that minimizes $\left\| \mathbf{B}\Delta\mathbf{A} - \Delta\mathbf{P}' \right\|^2$. Since the problem is in the standard form for weighted linear least squares, it can be readily shown that

$$\Delta\mathbf{A} = \left(\mathbf{B}^T \mathbf{C} \mathbf{B} \right)^{-1} \mathbf{B}^T \mathbf{C} \Delta\mathbf{P}'. \tag{4.6}$$

$\mathbf{C}$ is a 3N x 3N matrix of the reciprocals of the component-by-component paired covariances of $\mathbf{P}'_{k2}$-$\mathbf{P}'_{k1}$ for k=1,2...,N. The dominant error contribution in landmark locations is mutually independent random noise due to feature mismatch. We estimated the mismatch error to have a standard deviation of 1 km (2 km for N=151 case) along each spatial dimension. Therefore, $\mathbf{C}$ is the identity matrix with units of km^{-2}. This error model is consistent with the residual mis-registration errors observed in the determined spin model. See Figure 4.

In order to avoid errors due to the linear Taylor approximation, we reapply the linear fit iteratively until it converges. Each iteration in the fitting procedure is given by:

$$\mathbf{A}^{i+1} = \mathbf{A}^i + \mu\left(\mathbf{A}^i - \mathbf{A}^{i-1} \right) + (1-\mu)\Delta\mathbf{A}^i; \quad \Delta\mathbf{A}^i = \left(\left(\mathbf{B}^i\right)^T \mathbf{C}\mathbf{B}^i \right)^{-1} \left(\left(\mathbf{B}^i\right)^T \mathbf{C}\Delta\mathbf{P}'^i \right) \quad \mathbf{A}^{-1} = A^0 \tag{4.7}$$

In the first iteration, we compute $\Delta\mathbf{A}$ by (4.6) using $\mathbf{B}$ and $\Delta\mathbf{P}'$ matrices evaluated at $\mathbf{A}=\mathbf{A}^0$. In each successive iteration, we apply $\Delta\mathbf{A}$ to update $\mathbf{A}$, recompute the $\mathbf{B}$ and $\Delta\mathbf{P}'$ matrices for the updated value of $\mathbf{A}$ and then repeat the estimation of $\Delta\mathbf{A}$. A momentum term μ=0.9 is employed each time $\mathbf{A}$ is updated to avoid converging to local minima. We typically run 200 iterations, but the solution converges within 20. After the final iteration we compute the covariance matrix of $\Delta\mathbf{A} = \left(\mathbf{B}^T \mathbf{C} \mathbf{B} \right)^{-1}$. The error bars on the spin parameters and the correlation among pairs of parameters are computed from the covariance matrix in the usual manner.

5 Estimated Spin Model

Using the technique described in the previous section we have obtained estimates of Titan's spin state parameters and their error bars, as shown in the following table. Also depicted are the nominal IAU Titan values (Davies et al. 1989) for these parameters and the differences between the two. All parameter values were estimated at 19:16:25 UTC Aug 1, 2006, a time midway through our observed data.

Parameter	Estimate ± 1σ N=50 case (N=151 case)	Nominal value (IAU TITAN)	Estimated - Nominal
Pole_RA (deg)	39.483 ± 0.025 (39.470 ± 0.032)	37.589	1.894 (1.881)
Pole_DEC (deg)	83.4279 ± 0.0024 (83.4321 ± 0.0031)	83.6710	-0.2431 (-0.2479)
Spin Rate (deg/day)	22.57809 ± 0.00011 (22.57790 ± 0.00013)	22.5770	0.0011 (0.0009)
dPRA/dt (deg/century)	-30.1 ± 4.2 (-25.2 ± 4.9)	-2.2031	-27.9 (-23.2)
dPD/dt (deg/century)	-0.05 ± 0.36 (0.27 ± 0.44)	-0.1252	0.0752 (0.3952)
dSR/dt (deg/day/century)	0.0523 ± 0.0050 (0.0395 ± 0.0066)	0.0000	0.0523 (0.0395)

Table 1: Estimated Titan pole and spin rate parameters with error bars.

We observe statistically significant differences from the nominal case for five of the six parameters. The only exception is the derivative of pole declination, which is not significantly different from the nominal value or from zero. The angle between the estimated pole location vector and the nominal vector is 0.3230 deg. (The large difference in right ascension is somewhat misleading because small angle changes in the pole near 90 degrees declination can result in large changes in right ascension.)

Our confidence in the change in pole location is very high. The measured change is greater than 80 times the standard error. The spin rate is asynchronous by 0.001 deg/day and is currently becoming more asynchronous. Our confidence in this result is less than that of the pole location, but it is still significant. The spin rate change is 9 times larger than its standard error, and the change in the derivative of spin rate is 10 times larger. The rate of change of pole right ascension is a factor of 7 larger than its standard error and a factor of 10 larger than the nominal value. This is arguably the most profound result as it indicates much more movement in the pole than previously expected. The correlation matrix from our least squares estimate, shown below, reveals significant correlation between certain pairs of parameters. In particular, the derivative of pole right ascension is highly correlated with spin rate. In the next section, we exhibit 2-D cuts of the parameter space to show the impact of this correlation.

	DEC	RA	Spin	dDEC	dRA	dSpin
DEC	1	-0.09	0.13	-0.017	-0.078	-0.29

RA	-0.09	1	0.64	-0.24	-0.62	-0.18
Spin	0.013	0.64	1	-0.34	-0.98	-0.20
dDEC	-0.017	-0.24	-0.34	1	0.32	-0.056
dRA	-0.078	-0.62	-0.98	0.32	1	0.39
dSpin	-0.29	-0.18	-0.20	0.056	0.39	1

Table 2: Correlation coefficients between pairs of spin model parameters.

6 Geophysical Implications

One conclusion that can be drawn from our results is that Titan closely follows but departs slightly from a Cassini state, an equilibrium spin orientation induced by only gravitational torque. We derive this result from the location of the pole . To be in a Cassini state, the spin axis, orbit normal and the normal to the Laplace plane must be coplanar (Colombo 1966, Yseboodt & Margot 2006). The IAU Titan pole location is itself an estimate of the orbit normal (Davies et al. 1989, Jacobson et al. 2004), because zero obliquity was presumed in its derivation. The normal to the Laplace plane is the center about which the orbit normal is precessing (RA,DEC)=(36.226,83.966) (Margot 2008). The best fit pole location is 0.091 degrees (25 standard errors) removed from the plane formed by the orbit normal and the normal to the Laplace plane. Barring large errors in the IAU estimates of the orbit normal and/or the normal to the Laplace plane, we can rule out Titan being exactly in a Cassini state. The Laplace normal is by far the more likely error source, but it would have to be off by 30% of the estimated radius of precession for the three vectors to be coplanar. Titan is almost certainly locked in a 1 to 1 spin/orbit resonance. If it were not, we would expect the spin axis to be randomly oriented about the orbit normal. Our data is consistent with the spin axis lagging or oscillating about the exact Cassini state. Data over a longer time period is required to determine precisely how the relationship between the observed spin orientation and the Cassini state varies over time. We can conclude from the observed deviation from the Cassini state that Titan is not exactly in rotational equilibrium and/or there is a non-negligible torque other than the gravitational influence of Saturn. If Titan's spin state is not in equilibrium, the only obvious explanation is a large recent impact. No such event has been identified on Titan. If Titan's spin state is in equilibrium, then it is necessary to look for other torque candidates. Seasonal variations in Titan's rotation rate, about a long-term synchronous mean, have been predicted to arise from surface-atmosphere angular momentum exchange in the presence of an internal ocean (Tokano & Neubauer 2005). The implications of our measurements in this context are discussed more fully in a separate paper (Lorenz et al. 2008).

7 Validation

Four methods were used to validate our Titan spin model. First we repeated the fitting procedure on subsets of the data and examined the results. We found that our results were self-consistent. The differences among the fits for the various data subsets were in agreement with their estimated error

bars. Figure 2, below, depicts the pole location estimate for three different data subsets as compared with the nominal pole. The first case only used 3 sets of overlapping SAR images, T16/T19, TA/T23, and T16/T19 for a total of 14 landmarks. For this case we used a spin rate independent fitting procedure to directly estimate the plane of rotation without minimizing co-registration error. The other two cases employed a progressively larger number of overlapping regions and landmarks using the technique described in section 2. Despite using two different techniques and three different data sets, the pole location estimate varied very little.
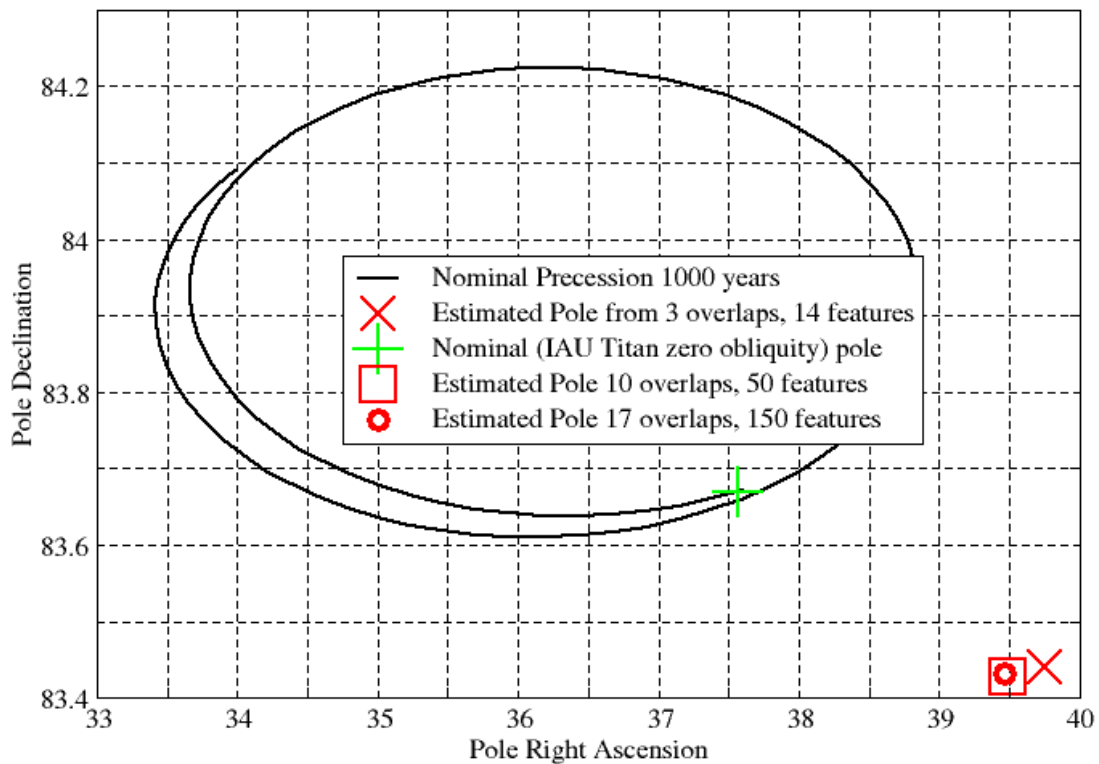
Figure 2: Comparison of nominal IAU Titan spin axis and several versions of the estimated North pole of Titan. The pole was estimated using 14, 50, and 151 features. The resultant estimated locations (three red symbols) are tightly grouped together, especially when compared to the nominal location (green cross). Because the IAU Titan spin model was developed with a presumption of zero obliquity the IAU Titan spin axis is the same as the orbit normal. All four pole locations depicted are at time 19:16:25 UTC Aug 1 2006.

Our second validation approach was a Monte Carlo simulation of the fitting procedure. Simulated landmark locations were obtained utilizing various candidate spin models as truth including our

estimated model and IAU Titan. For each L_k, the inertial location from the image obtained at time t_{k1} from the real data was used as the true position. The t_{k2} location was computed from the candidate spin model with 1 km Gaussian noise added to each spatial component to simulate landmark mismatching error. The fitting procedure was then applied in the usual manner. The differences between the candidate spin model parameters and the estimated quantities were consistent with the postfit error bars.

The third check we applied was to compute 2-D cuts of co-registration error in the 6-D spin parameter space. Figure 3 depicts one such cut that demonstrates the coupling between spin rate, ω, and the rate of change in pole right ascension, $\dot{\phi}$. An exhaustive search was performed in the three dimensions of $\dot{\phi}$, ω and $\dot{\omega}$. We found no extraneous solutions.
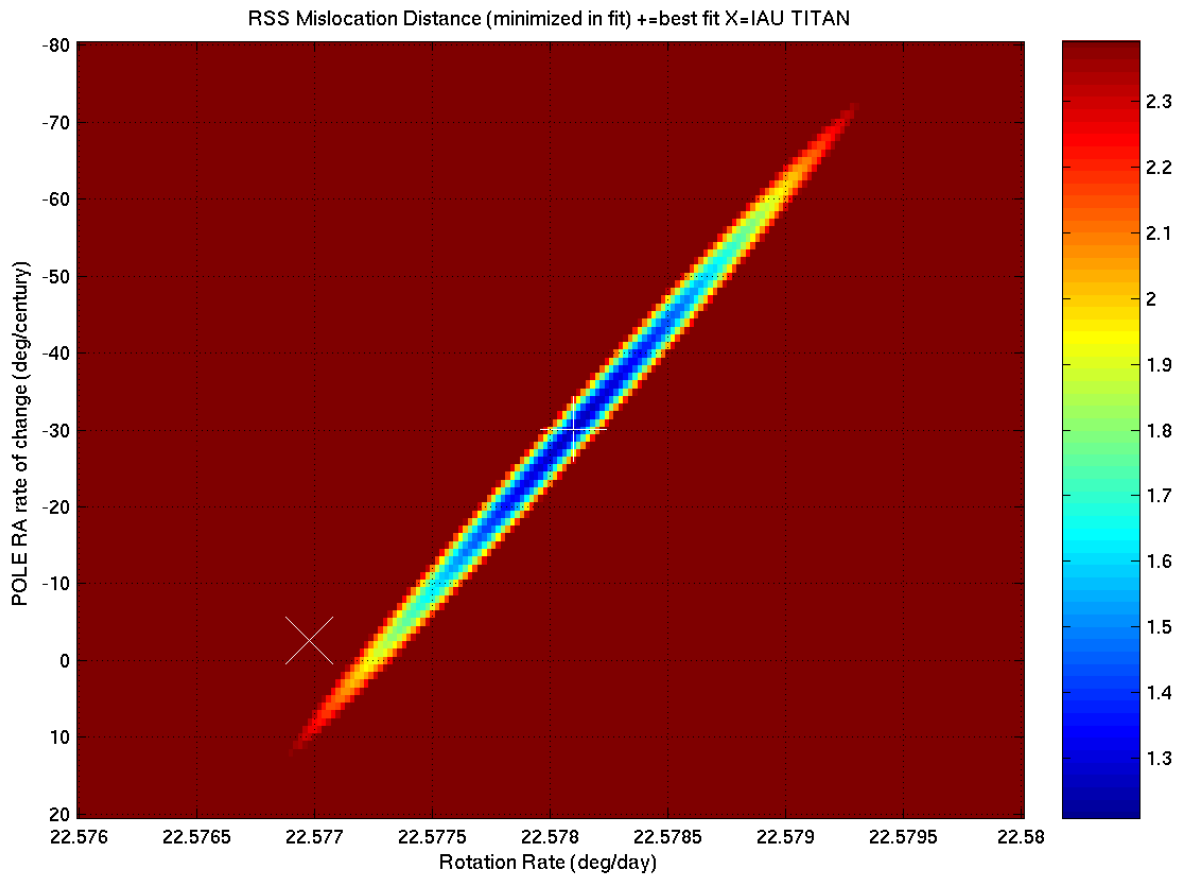
Figure 3: Goodness of fit pseudo-color map for derivative of POLE_RA and spin rate. The goodness of fit metric is E_{tot}/N. The x-axis is spin rate. The y-axis is rate of change in pole right ascension. The color scale goes from dark blue = 1.2 km to dark red > 2.4 km. The X indicates the synchronous no pole wobble case. Due to correlation between the two parameters, the locus of good fits is elongated.
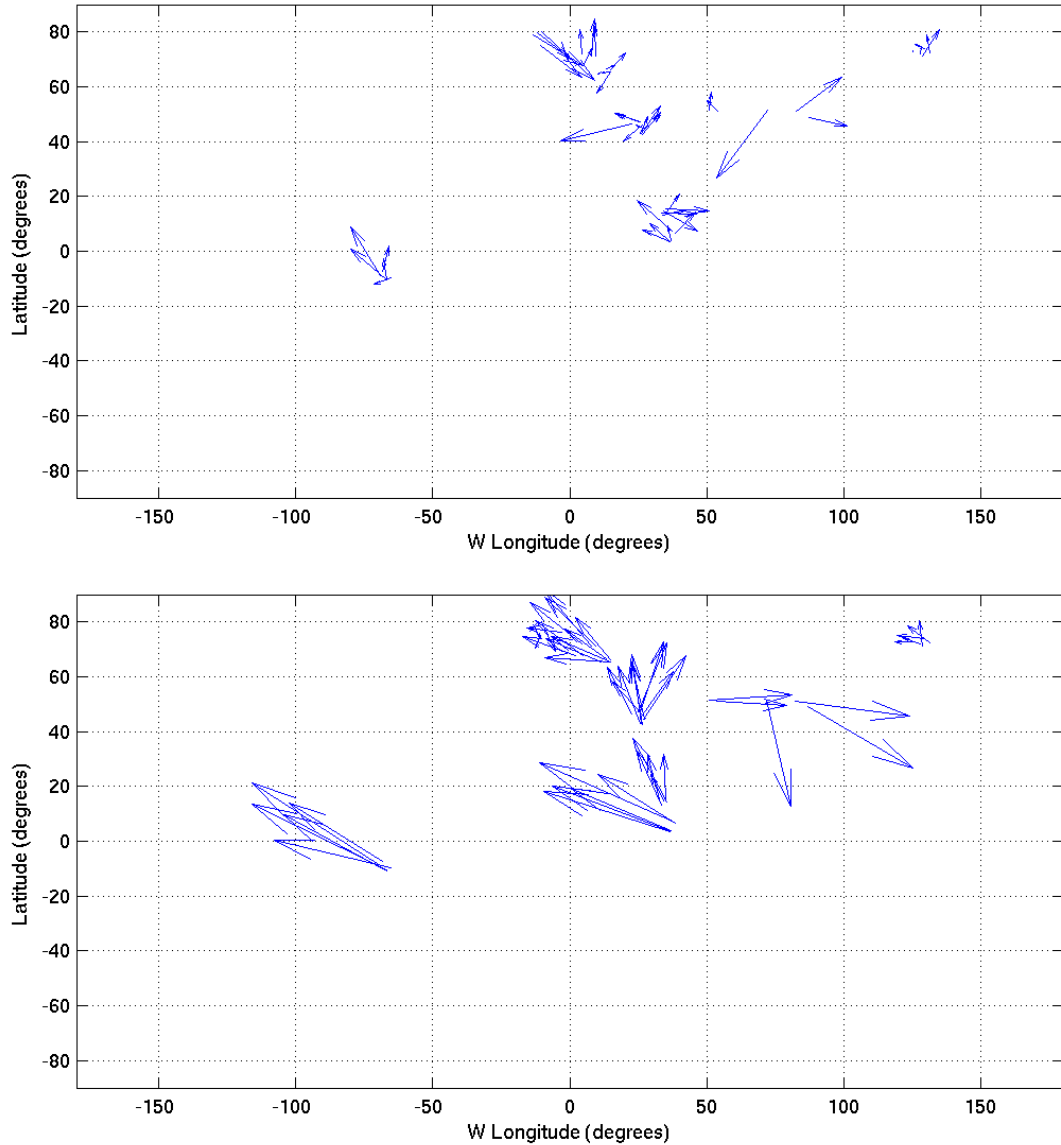
Figure 4: Landmark misregistration error vs. latitude and longitude plots for overall best fit (top) and best fit constrained to have constant, synchronous spin rate and no pole wobble (bottom). Vector lengths are in units of 100 m, so that a vector that extends across twenty degrees on the plot actually represents a 2 km error. The tail of the arrow corresponds to the location of the first observation of each landmark. The direction of the arrow is the direction of apparent change in the landmark location. Clearly, including spin rate and pole change parameters improves the fit in a systematic manner.

Our fourth check was to explore fits excluding some of the parameters to address the effect of systematic biases in the locations. Figure 4 graphically depicts the residual location errors for two cases: the full six-parameter fit and the best fit with constant, synchronous spin rate and no pole wobble. For each fit, the random and systematic error components of the residual misregistration error were computed. Systematic error e_{sys} is the root sum square of the average misregistration

error for landmarks L_k in each region R_j where a pair of SAR observations overlaps. The random component e_{rand} is the remaining error when the systematic component is removed.

$$e_{sys} = \sqrt{\frac{1}{N}\sum_{j=1}^{M}\left\|\sum_{k,L_k \in R_j} E_k\right\|^2}\; ; \quad e_{rand} = \sqrt{\frac{E_{tot}}{N} - e_{sys}^2}$$

These quantities were computed to address the impact of systematic errors in our inputs. The error bars we computed during the fitting procedure are based on the assumption that errors in the locations of the landmarks are random, with 1 km standard deviation in each component. If this error model is valid, then so are the error bars. Even if the standard deviation were 2 or 3 times larger, our results would still be statistically significant because the refinements we observe in each parameter are at least seven times its standard error. The N=151 case, which has approximately twice the random feature mismatch error of the N=50 case, resulted in a very similar fit. The magnitude of the differences in the parameters for the two fits is consistent with the error bars.

On the other hand, large systematic errors in our landmark locations could impact the accuracy of parameter estimates. This problem is exemplified by the fit performed using a spherical Titan. We utilized an estimate of Titan surface heights from SAR data during the computation of landmark locations (Stiles et al. 2007a, 2007b). The standard deviation of the estimated heights from the 2,575 km reference sphere is 506 m. The heights are not randomly distributed; they exhibit latitude dependence. When we leave these heights out of the location computation and assume a spherical Titan, our fit gets worse, e_{sys} increases from 0.9273 to 1.9059 km, and more importantly we see a change in the parameters. Five of the parameters do not change significantly, but the rate of change in declination changes to -2.0 deg/century. This value is 6 times the reported error bar. Latitude dependent surface height errors mimic an error in declination, resulting in the erroneous fit. The problem with the spherical Titan fit indicates the need to examine systematic input error. For the spherical Titan case, there are two indicators that diagnose problems with the fit: the large e_{sys} value itself and the insensitivity of e_{sys} and E_{tot} to parameter changes. Setting $\dot{\omega}=0$ only increases e_{sys} from 1.9059 to 2.0485 km. Such a small change in e_{sys} indicates $\dot{\omega}$ has little impact on the fit and we should thus have little confidence in its value.

Table 3 depicts e_{sys} and e_{rand} for the IAU Titan model, the best pole location fit with all other parameters set to their nominal values, the best fit with a presumed spherical Titan, the best fit for each of $\dot{\phi}$, ω and $\dot{\omega}$ parameters set to its nominal value, and the best overall fit to all 6 parameters.

Error Metric	IAU Titan	Best Fit Pole Location only	Best Fit for spherical Titan	Best Fit constant spin rate	Best Fit sync. spin rate	Best Fit no pole wobble	Best Overall Fit
e_{rand}(km)	0.9795	0.8695	0.9276	0.8875	0.8970	0.8766	0.8591
e_{sys} (km)	18.7639	2.5489	1.9059	1.7396	1.6250	1.3084	0.9273

Table 3: Random and systematic error residuals for various fits.

All the various fits have similar values for e_{rand}. But the e_{sys} values vary considerably. The best fit for all six parameters produces the lowest e_{sys} value. The nominal IAU Titan model has 18.8 km of systematic misregistration error. Fitting only the pole location while presuming a constant synchronous spin rate with no pole wobble yields e_{sys}=2.54 km. Omitting any single parameter from the fit increases e_{sys}. The parameter with the least impact is the derivative of right ascension. Setting $\dot{\phi}$=0 increases e_{sys} from 0.9273 to 1.3084 km.

There are five potential sources of systematic error in the landmark locations: Titan-relative spacecraft position, Titan-relative spacecraft velocity, height of surface, transmit frequency, and echo delay. Errors in echo delay, transmit frequency, spacecraft velocity, and spacecraft position are small, resulting in < 100 m errors in location. To test the effect of 100-m errors, we applied a 100 m standard deviation Gaussian noise term to each of the X, Y, and Z components of the s/c positions. The noise value was held constant within a flyby in order to simulate a systematic bias. (Random error for each landmark would have less effect on the parameter estimation.) The parameters estimated changed very little due to the added noise. POLE_RA increased by 0.007 degrees. POLE_DEC increased by 0.0024 degrees. Spin rate increased by 0.000011 deg/day. The derivative of RA decreased by 0.16 deg/century. The derivative of POLE_DEC increased by 0.114 deg/century. The derivative of spin rate decreased by 0.0006 deg/day/century. All of these changes are within the 1-sigma error bars; therefore, of the five sources of systematic error only height error is significant.

The residual error in height has a systematic error component with $\approx$200 m standard deviation (Stiles et al. 2007a, 2007b). A multiplicative effect due to incidence angle transforms a 200 m height error into a 400-500 m error in pixel location. We can thus reject the constant spin rate and synchronous spin rate hypotheses because they increase e_{sys} by 812 m and 698 m, respectively. The no-pole-wobble case with a 381 m increase is also unlikely. Even though a systematic mislocation error > 400 m is possible, it is extremely unlikely that one could achieve a 381 m decrease in e_{sys} by fitting to a systematic height error. In the spherical Titan fit, a 500 m systematic height error induced an additional 1 km in e_{sys}. The fitting procedure modified the parameters in the attempt to fit to the systematic error, but the resultant decrease in e_{sys} was only 216 m. Given the factor of two reduction in height errors from the spherical assumption, the 381 m decrease in e_{sys} due to pole wobble appears to be 3 times too large to be a spurious fit due to height error. The original height errors due to assuming a spherical Titan varied with latitude in a manner that mimicked declination error; the current residual heights are unlikely to have such a bias. Even the spherical Titan assumption only impacts the rate of change in the pole location without substantially affecting the other parameters. For a further description of the method used to estimate surface heights and its effect on our analysis see Appendix section A.3.

8 Conclusions

We have estimated quantities for five of the parameters comprising the spin state of Titan with varying degrees of confidence. We have estimated a new pole position with an obliquity of 0.3 degrees. The observed change in pole position from the nominal value is 80 times its standard error. Without invoking this pole position, landmark features are displaced in repeat imaging by

some 20 km. We have also estimated that the spin rate is currently 0.001 deg/day faster than synchronous and is increasing at a rate of 0.05 deg/day/century and that the pole right ascension is currently decreasing at a rate of -30 deg/century. These conclusions taken together are also highly certain; the best fit with constant, synchronous rotation and no pole wobble leaves systematic 2.5 km landmark mislocations unexplained. Individually, each parameter is statistically significant given random error assumptions. Systematic errors in surface height are the largest known source of error in the fits. Residual height errors are unlikely to change any of the conclusions so long as we use the height estimates derived from the SAR data itself (Stiles et al. 2007a, 2007b) rather than a spherical Titan approximation.

We conclude that Titan is close to an exact Cassini state, but not precisely in that state. This conclusion can be derived from the pole location, our strongest result. Titan is either not in an equilibrium spin state or is undergoing significant non-gravitational torque such as that described in (Tokano & Neubauer 2005, Lorenz et al. 2008).

9 Acknowledgement

10 References

Colombo, G., "Cassini's Second and Third Laws," The Astronomical Journal, Vol. 71, No. 9, pp. 891-896, 1966.

Davies, M.E., et al., "Report of the IAU/IAG/COSPAR Working Group on Cartographic Coordinates and Rotational Elements of the Planets and Satellites," Celestial Mechanics and Dynamical Astronomy 46: 187-204, 1989.

Davies, M. E, et al., "The Rotational Period, Direction of the North-Pole and Geodetic Control Network of Venus," Journal of Geophys. Res. -Planets, Volume 97 (E8): 13141-13151 Aug 25, 1992.

Jacobson, R. A., et al., "The orbits of the major Saturnian satellites and the gravity field of the Saturnian system," BAAS 36 (4) 1097, 36th Meeting of the American Astronomical Society Division for Planetary Sciences, 2004.

Lorenz, R, et al., "Titan's Changing Length of Day: Cassini RADAR Evidence of an Internal Water Ocean and Seasonal Variation of Atmospheric Angular Momentum," accepted for publication in Science, 2008.

Margot, J.-L., Personal Communication, 2008.

Stiles, B.W., Hensley, S., Gim, Y., Kirk, R., Zebker, H., Janssen, M., and the Cassini RADAR Team, "Estimating Titan Surface Topography from Cassini Synthetic Aperture RADAR Data," American Geophysical Union 2007 Fall Meeting, San Francisco, CA, 2007a.

Stiles, B.W., et al., "Coincident Surface Topography Measurements and SAR Imagery of Titan," in preparation, 2007b.

Tokano, T. and Neubauer, F. M., "Wind-induced seasonal angular momentum exchange at Titan's surface and its influence on Titan's length-of-day," Geophysical Research Letters, Vol. 32, 2005.

Yseboodt, M. and Margot, J-L., "Evolution of Mercury's obliquity," Icarus Vol. 181, pp. 327-337, 2006.

A. Appendix

A.1 Description of Timing of Cassini Radar Data

The more astute reader will realize that SAR observations are not instantaneous. Each landmark is observed over some duration during which Doppler and range vary as a function of time. Cassini SAR is a special case for which measurement durations may be ignored. Cassini SAR employs a burst-mode timing scheme. Many SAR systems operate in a continuous mode, which means that a train of chirped pulses is transmitted with regular time interval throughout the observation period. The interval between the pulses is such that returned echoes can be obtained between the transmitted pulses. The collection of pulses that contain reflected energy within the radar antenna's main lobe is processed in a coherent manner to obtain high along-track resolution in the resulting SAR image. Data rate and data volume constraints make a continuous mode design unsuitable for the wide area coverage desired for the surface of Titan. Instead the Cassini radar utilizes a burst-mode SAR in which a train (burst) of 30-60 chirped pulses is transmitted followed by a long gap (about 400-800 pulse intervals in length) in transmission lasting until the return echo from the burst is received. After reception of the echo, the cycle repeats. Each individual burst impinges on the surface of Titan for less than 0.1 s. For this reason, we do not need to account for variation in range or Doppler during a burst in either the Cassini SAR processor itself or in determining the spin state of Titan. Up to 20 consecutive pulse trains (bursts) can observe the same landmark for a total maximum duration of 40 s. Each of these bursts observes a given landmark at a slightly different time from a slightly different Doppler and range. Single look SAR imagery from multiple bursts are interpolated and incoherently averaged to obtain the final SAR image. For our purposes we only consider the time, Doppler, and range of the central burst in the collection. If the IAU Titan spin model used in the SAR processing correctly described the spin state of Titan this approximation would be identically correct. The Doppler, range, and time triplets of all the individual bursts would then correspond to the exact same position on the surface of Titan and could thus be used interchangeably. Errors in the spin state, such as those we have observed in this paper, induce a slight spreading in the actual surface locations observed by the collection of bursts. This spreading tends to defocus the image. The error is small and we do not observe any such defocusing in the Cassini SAR imagery. A 1.5-degree error in the North pole of Titan (5 times larger than what we observe) would result in a maximal rate of change of 0.33 m/s in the apparent position of a landmark on Titan's surface. Over the 40 s maximal observation duration, the apparent surface position changes by less than 14 m. For this reason we need only consider the central burst obtained during each landmark observation.

A.2 Landmark Data Set

The following tables contain the information we used to estimate our fits from the 50-landmark data set. Table A.1 contains the time, carrier signal wavelength, range from spacecraft to target, Doppler shift of the returned echo, and SARTopo surface height estimate for the first observation of each of the 50 landmarks. Time is reported as seconds since 12:00 TT January 1, 2000. Table A.2 contains the same information for the second observation with the addition of the SARTopo surface height estimate. The surface height was presumed to be the same for both observations. The quantity used in the analysis was the closest SARTopo measurement to the landmark in the second flyby. The second flyby was chosen to eliminate early flybys such as TA and T3 in which poorer spacecraft attitude may have yielded a less accurate height estimate. Table A.3 contains the spacecraft ephemeris (position and velocity in the Titan-centered inertial frame) for the first observation of each landmark. Table A.4 contains the spacecraft ephemeris for the second observation of each landmark.

Landmark ID	time(s)	wavelength(cm)	range(km)	Doppler(Hz)
tat23_p1	152076775.3	2.17405	1352.08	-101374
tat23_p2	152076734.7	2.17405	1291.20	-66374
tat23_p3	152076854.8	2.17404	1438.19	-165010
tat23_p4	152077020.5	2.17398	1805.30	-262499
tat23_p5	152077005.3	2.17398	1751.45	-263764
tat25_p1	152077345.4	2.17396	2930.60	-397589
tat25_p2	152077344.4	2.17396	2946.68	-396999
tat25_p3	152077319.5	2.17396	2860.69	-382729
tat25_p4	152077370.9	2.17396	3078.73	-395954
tat25_p5	152077328.6	2.17396	2901.66	-385158
t3t25_p1	161723235.5	2.17559	2570.56	-296821
t3t25_p2	161723239.7	2.17559	2594.55	-307526
t3t25_p3	161723279.5	2.17559	2739.00	-322127
t3t25_p4	161723282.1	2.17559	2734.73	-323371
t3t25_p5	161723220.0	2.17560	2510.89	-290180
t8t21_p1	183745642.5	2.17401	2947.19	-358010
t8t21_p2	183745645.2	2.17401	2963.37	-358743
t8t21_p3	183745596.7	2.17401	2748.42	-345366
t8t21_p4	183745629.7	2.17401	2858.70	-363044
t8t21_p5	183745695.9	2.17401	3149.21	-376694
t16t19_p1	206799763.4	2.17409	1302.94	184235
t16t19_p2	206799757.2	2.17409	1315.72	187688
t16t19_p3	206799756.9	2.17409	1292.25	199350
t16t19_p4	206799777.7	2.17409	1248.84	184345
t16t19_p5	206799778.0	2.17409	1282.59	172713

t16t25_p1	206800126.1	2.17404	1194.46	-126870
t16t25_p2	206800133.9	2.17404	1194.07	-142908
t16t25_p3	206800181.0	2.17404	1251.08	-180373
t16t25_p4	206800132.1	2.17404	1161.22	-141728
t16t25_p5	206800171.9	2.17404	1260.29	-163818
t17t25_p1	210932467.4	2.17564	1413.99	-908
t17t25_p2	210932465.7	2.17564	1422.72	352
t17t25_p3	210932462.4	2.17564	1411.07	-385
t17t25_p4	210932453.3	2.17564	1312.38	-1244
t17t25_p5	210932451.6	2.17564	1316.17	-11088
t18t25_p1	212309997.6	2.17564	1034.68	-1870
t18t25_p2	212310002.4	2.17564	1044.71	-2192
t18t25_p3	212310000.4	2.17564	1017.79	-11485
t18t25_p4	212310001.2	2.17564	1042.34	-2132
t18t25_p5	212310012.2	2.17564	1025.61	-11642
t19t25_p1	213686954.1	2.17408	1163.21	94245
t19t25_p2	213686903.9	2.17409	1268.92	147399
t19t25_p3	213686885.4	2.17409	1293.70	162599
t19t25_p4	213686891.3	2.17409	1287.11	157160
t19t25_p5	213686927.0	2.17408	1166.71	127213
t23t25_p1	221949293.3	2.17410	1420.67	227821
t23t25_p2	221949322.0	2.17410	1383.83	199339
t23t25_p3	221949312.1	2.17410	1391.12	216448
t23t25_p4	221949288.9	2.17410	1433.43	230712
t23t25_p5	221949314.6	2.17410	1384.62	214919

Table A.1: Time, carrier signal wavelength, range, and Doppler for the first observation of each landmark. Each landmark has a unique ID of the form txxtyy_pz where xx is the number of the first Titan flyby to observe the landmark, yy is the number of the second such flyby, and z is an integer between 1 and 5.

Landmark ID	time(s)	wavelength(cm)	range(km)	Doppler(Hz)	surface height(km)
tat23_p1	221948663.8	2.17413	3863.12	414256	-0.850
tat23_p2	221948605.0	2.17409	4172.20	417755	-0.078
tat23_p3	221948779.1	2.17413	3333.15	403977	-0.539
tat23_p4	221949025.9	2.17412	2281.08	353239	-0.322
tat23_p5	221948993.1	2.17412	2423.87	363268	-0.506
tat25_p1	225386134.3	2.17562	1237.39	-123073	-0.128
tat25_p2	225386151.6	2.17562	1257.20	-139856	-0.160
tat25_p3	225386165.6	2.17562	1270.08	-151731	-0.203
tat25_p4	225386161.3	2.17562	1211.87	-148048	-0.320
tat25_p5	225386173.7	2.17562	1273.76	-169867	-0.203

t3t25_p1	225385797.8	2.17567	1325.07	185804	-0.254
t3t25_p2	225385790.1	2.17567	1362.03	192129	-0.249
t3t25_p3	225385776.7	2.17567	1348.13	214131	-0.187
t3t25_p4	225385786.4	2.17567	1324.42	205712	-0.315
t3t25_p5	225385804.3	2.17567	1329.88	180266	-0.307
t8t21_p1	219196640.8	2.17400	3657.38	-417914	-0.240
t8t21_p2	219196647.5	2.17400	3689.65	-418455	-0.189
t8t21_p3	219196602.0	2.17400	3491.31	-415030	-0.169
t8t21_p4	219196585.1	2.17400	3403.33	-413616	-0.163
t8t21_p5	219196613.3	2.17400	3517.90	-409219	-0.240
t16t19_p1	213686521.9	2.17412	2214.89	354651	-0.644
t16t19_p2	213686512.7	2.17412	2248.94	357298	-0.609
t16t19_p3	213686536.4	2.17412	2172.99	341417	-0.657
t16t19_p4	213686565.0	2.17412	2071.41	330878	-0.512
t16t19_p5	213686543.8	2.17412	2129.76	347249	-0.377
t16t25_p1	225386509.9	2.17558	2206.36	-361369	-0.643
t16t25_p2	225386512.4	2.17558	2208.28	-362397	-0.735
t16t25_p3	225386485.5	2.17559	2057.55	-360732	-0.880
t16t25_p4	225386527.9	2.17558	2255.19	-368038	-0.616
t16t25_p5	225386478.3	2.17559	2042.86	-358164	-0.765
t17t25_p1	225385662.8	2.17568	1630.18	279179	-0.297
t17t25_p2	225385657.0	2.17569	1649.35	282404	-0.363
t17t25_p3	225385658.0	2.17569	1655.36	281369	-0.322
t17t25_p4	225385688.0	2.17568	1599.21	273456	-0.230
t17t25_p5	225385676.7	2.17568	1648.00	279678	-0.265
t18t25_p1	225386420.7	2.17559	1889.76	-322610	-0.792
t18t25_p2	225386408.9	2.17559	1843.67	-316801	-0.934
t18t25_p3	225386431.8	2.17559	1919.27	-327403	-0.815
t18t25_p4	225386411.1	2.17559	1852.45	-317245	-0.935
t18t25_p5	225386427.2	2.17559	1883.96	-334816	-0.972
t19t25_p1	225386620.4	2.17558	2607.55	-399457	-0.686
t19t25_p2	225386690.2	2.17558	2941.67	-415716	-0.465
t19t25_p3	225386705.2	2.17558	3029.66	-418100	-0.462
t19t25_p4	225386701.1	2.17558	3004.12	-417219	-0.462
t19t25_p5	225386622.3	2.17558	2648.68	-399324	-0.846
t23t25_p1	225386134.3	2.17562	1237.39	-123073	-0.128
t23t25_p2	225386116.1	2.17562	1194.64	-118146	0.016
t23t25_p3	225386125.5	2.17562	1201.30	-127961	-0.006
t23t25_p4	225386135.0	2.17562	1246.87	-124400	-0.128
t23t25_p5	225386124.5	2.17562	1194.91	-126465	0.031

Table A.2: Time, carrier signal wavelength, range, Doppler, and estimated surface height for the second observation of each landmark. Surface height is km above a reference sphere of radius 2575 km centered upon Titan's center of gravity.

| Landmark ID | Spacecraft Position(km) | | | Spacecraft Velocity | | |
	x	y	z	(km/s) x	y	z
tat23_p1	2923.688	1082.087	2173.677	-1.665159	5.721882	1.070991
tat23_p2	2991.038	849.137	2129.805	-1.645206	5.728394	1.085508
tat23_p3	2789.894	1536.220	2257.684	-1.700974	5.705518	1.043229
tat23_p4	2502.834	2478.244	2426.145	-1.759620	5.661641	0.991541
tat23_p5	2529.628	2391.892	2410.995	-1.755150	5.665964	0.995837
tat25_p1	1919.887	4302.666	2735.967	-1.819773	5.573871	0.922929
tat25_p2	1921.689	4297.148	2735.053	-1.819667	5.574107	0.923080
tat25_p3	1966.875	4158.554	2712.066	-1.816898	5.580122	0.926959
tat25_p4	1873.358	4445.003	2759.499	-1.822387	5.567852	0.919143
tat25_p5	1950.441	4209.001	2720.442	-1.817932	5.577916	0.925525
t3t25_p1	1979.344	4335.632	1670.258	-2.881077	5.138333	-0.030334
t3t25_p2	1967.475	4356.795	1670.132	-2.881642	5.137091	-0.030812
t3t25_p3	1852.526	4561.294	1668.814	-2.886709	5.125282	-0.035239
t3t25_p4	1845.095	4574.485	1668.723	-2.887013	5.124533	-0.035513
t3t25_p5	2024.148	4255.658	1670.715	-2.878872	5.143059	-0.028494
t8t21_p1	-5032.599	996.252	394.826	-2.110447	5.431706	-0.179901
t8t21_p2	-5038.338	011.025	394.337	-2.109680	5.431401	-0.179961
t8t21_p3	-4935.601	747.273	403.045	-2.123926	5.436758	-0.178822
t8t21_p4	-5005.510	926.584	397.132	-2.114112	5.433136	-0.179612
t8t21_p5	-5144.974	286.320	385.183	-2.096037	5.425657	-0.181007
t16t19_p1	725.023	-13.930	3689.088	5.546604	1.904736	-0.938019
t16t19_p2	758.965	-25.587	3694.817	5.545842	1.904716	-0.934220
t16t19_p3	760.741	-26.197	3695.116	5.545801	1.904715	-0.934023
t16t19_p4	645.546	13.359	3675.585	5.548280	1.904737	-0.947033
t16t19_p5	643.881	13.930	3675.300	5.548314	1.904736	-0.947224
t16t25_p1	287.209	674.129	3304.017	5.525122	1.880761	-1.185871
t16t25_p2	330.557	688.883	3294.692	5.523169	1.879743	-1.190794
t16t25_p3	590.148	777.183	3237.986	5.510523	1.873391	-1.219109
t16t25_p4	320.465	685.448	3296.866	5.523628	1.879981	-1.189653
t16t25_p5	540.211	760.204	3249.008	5.513072	1.874643	-1.213825
t17t25_p1	2650.704	-2395.134	108.785	5.207172	2.298542	-1.759242
t17t25_p2	2642.060	-2398.949	1111.705	5.207926	2.297858	-1.758925
t17t25_p3	2624.902	-2406.516	117.498	5.209421	2.296494	-1.758293
t17t25_p4	2577.653	-2427.319	133.431	5.213517	2.292687	-1.756520
t17t25_p5	2568.476	-2431.354	136.523	5.214309	2.291939	-1.756170
t18t25_p1	463.394	174.954	3212.929	4.870736	2.549088	-2.315128
t18t25_p2	486.965	187.291	3201.716	4.869284	2.548909	-2.318284
t18t25_p3	476.948	182.048	3206.483	4.869904	2.548987	-2.316944
t18t25_p4	481.073	184.207	3204.521	4.869649	2.548955	-2.317496
t18t25_p5	534.674	212.271	3178.964	4.866274	2.548509	-2.324636

Landmark ID	x	y	z	vx	vy	vz
t19t25_p1	1471.805	-195.402	3300.273	4.476097	2.511145	-3.029409
t19t25_p2	1246.751	-321.420	3451.579	4.488713	2.508754	-2.998102
t19t25_p3	1163.930	-367.679	3506.767	4.492659	2.507626	-2.986712
t19t25_p4	1190.522	-352.833	3489.075	4.491432	2.508002	-2.990358
t19t25_p5	1350.759	-263.240	3381.901	4.483231	2.509987	-3.012525
t23t25_p1	2493.960	-837.451	2915.498	2.607973	2.450775	-4.725768
t23t25_p2	2568.579	-767.132	2779.824	2.596937	2.454273	-4.738186
t23t25_p3	2542.818	-791.453	2826.767	2.600852	2.453079	-4.733890
t23t25_p4	2482.416	-848.294	2936.405	2.609598	2.450225	-4.723856
t23t25_p5	2549.371	-785.271	2814.837	2.599866	2.453384	-4.734982

Table A.3: Inertial spacecraft position and velocity during the first observation of each landmark. Vectors are in the J2000 coordinate system with the origin at Titan's center of gravity.

Landmark ID	Spacecraft Position(km)			Spacecraft Velocity		
	x	y	z	(km/s) x	y	z
tat23_p1	811.743	-2356.012	818.229	2.701623	2.378904	-4.521768
tat23_p2	652.924	-2495.680	083.627	2.703055	2.374170	-4.510153
tat23_p3	1123.147	-2081.016	5295.177	2.697080	2.389233	-4.547657
tat23_p4	1786.302	-1488.271	164.657	2.674143	2.416334	-4.619825
tat23_p5	1698.556	-1567.424	315.932	2.678689	2.412349	-4.608761
tat25_p1	-2353.446	1070.870	2582.240	2.229703	-2.939060	5.013018
tat25_p2	-2314.723	1019.882	2669.086	2.237079	-2.942365	5.004717
tat25_p3	-2283.442	978.775	2738.929	2.242827	-2.944864	4.997953
tat25_p4	-2292.999	991.327	2717.618	2.241091	-2.944116	5.000024
tat25_p5	-2265.302	954.969	2779.307	2.246073	-2.946244	4.994012
t3t25_p1	-3075.650	044.790	873.399	2.058384	-2.841063	5.123447
t3t25_p2	-3091.397	066.534	834.164	2.054531	-2.838493	5.124514
t3t25_p3	-3118.933	104.610	765.357	2.047846	-2.834001	5.126237
t3t25_p4	-3098.954	076.978	815.305	2.052690	-2.837260	5.125005
t3t25_p5	-3062.153	026.168	906.964	2.061703	-2.843265	5.122484
t8t21_p1	3341.256	5060.907	-1237.306	3.417355	2.443710	-3.953210
t8t21_p2	3364.405	5077.458	-1264.088	3.416502	2.442418	-3.952892
t8t21_p3	3208.519	4965.910	-1083.833	3.422380	2.451414	-3.954992
t8t21_p4	3150.894	4924.618	-1017.256	3.424634	2.454924	-3.955737
t8t21_p5	3247.464	4993.798	-1128.846	3.420882	2.449099	-3.954478
t16t19_p1	-475.780	-1273.264	556.293	4.513363	2.472034	-2.802088
t16t19_p2	-517.008	-1295.841	581.874	4.512989	2.471064	-2.798640
t16t19_p3	-410.302	-1237.391	515.604	4.513909	2.473582	-2.807682
t16t19_p4	-281.248	-1166.635	435.177	4.514791	2.476657	-2.819132
t16t19_p5	-376.659	-1218.953	494.667	4.514164	2.474381	-2.810612
t16t25_p1	-1493.391	-40.956	4431.184	2.330847	-2.968917	4.839235

t16t25_p2	-1487.400	-48.587	4443.619	2.331182	-2.968906	4.838237
t16t25_p3	-1550.031	31.241	4313.388	2.327500	-2.968927	4.848858
t16t25_p4	-1451.379	-94.441	4518.301	2.333123	-2.968812	4.832313
t16t25_p5	-1566.925	52.795	4278.175	2.326436	-2.968898	4.851793
t17t25_p1	-3349.044	425.178	181.116	1.995390	-2.797295	5.134103
t17t25_p2	-3360.591	441.372	151.385	1.992947	-2.795522	5.134224
t17t25_p3	-3358.598	438.576	156.519	1.993367	-2.795828	5.134205
t17t25_p4	-3298.698	354.693	310.295	2.006271	-2.805123	5.133297
t17t25_p5	-3321.327	386.350	252.323	2.001335	-2.801586	5.133717
t18t25_p1	-1700.579	223.679	3998.196	2.316854	-2.968077	4.876041
t18t25_p2	-1727.849	258.630	3940.745	2.314623	-2.967763	4.881210
t18t25_p3	-1674.851	190.732	4052.293	2.318869	-2.968324	4.871232
t18t25_p4	-1722.919	252.309	3951.141	2.315034	-2.967824	4.880270
t18t25_p5	-1685.659	204.570	4029.579	2.318033	-2.968226	4.873245
t19t25_p1	-1234.957	-369.183	4964.041	2.342460	-2.967239	4.799479
t19t25_p2	-1071.419	-576.046	5297.972	2.347375	-2.965238	4.777642
t19t25_p3	-1036.239	-620.473	5369.527	2.348240	-2.964746	4.773255
t19t25_p4	-1045.819	-608.377	5350.050	2.348011	-2.964882	4.774439
t19t25_p5	-1230.513	-374.812	4973.145	2.342615	-2.967192	4.798853
t23t25_p1	-2353.446	1070.870	2582.240	2.229703	-2.939060	5.013018
t23t25_p2	-2393.832	1124.165	2491.202	2.221710	-2.935364	5.021565
t23t25_p3	-2373.017	1096.682	2538.183	2.225867	-2.937301	5.017176
t23t25_p4	-2351.841	1068.754	2585.849	2.230014	-2.939202	5.012676
t23t25_p5	-2375.261	1099.642	2533.125	2.225423	-2.937096	5.017651

Table A.4: Inertial spacecraft position and velocity during the second observation of each landmark. Vectors are in the J2000 coordinate system with the origin at Titan's center of gravity.

A.3 Summary of SARTopo height estimation technique and its effect on our spin parameter fits.

The SARTopo surface height estimates are obtained by an Amplitude Monopulse Comparison Technique that makes use of data in which the same scene is observed by multiple beams (antenna feeds). This overlap is much different than what is used in the spin state study described in this paper. Instead of comparing SAR imagery from months or years apart, we compare imagery from adjacent beams obtained within seconds of each other. Using our knowledge of the antenna pointing and precise spacecraft ephemeris and attitude telemetry, we estimate the surface height for which two overlapping beams produce the same NRCS estimate. When the height used in the calibration is inaccurate, the errors in the calibration of the two beams are nearly equal and have opposite sign. When we get the same NRCS we know we have the correct height. We have compared the SARTopo data with co-located conventional nadir-pointing altimetry. In particular, we obtained closest approach nadir altimetry for Titan flyby T30. For a thousand km long region, the T30 altimetry and T28 SARTopo lined up within 5-10 km on the ground. For this 1000 km

stretch, we achieved 150 m bias and 60 m standard difference between the two height profiles. Also, the fact that we achieve a better residual mislocation error in the spin parameter fit is itself an independent validation of the SARTopo technique.

When we use a 2575 km spherical Titan (SPHER) assumption, we get the following fit to the 50 data point set. The best fit using the SARTopo is also shown for comparison.

Parameter	SPHER	SARTopo
POLE_RA(degrees)	39.505	39.483
POLE_DEC(degrees)	83.4221	83.4279
SPIN_RATE (deg/day)	22.5784	22.5781
Derivative of spin rate (deg/day/century)	0.0466	0.0523
Derivative of POLE_RA (deg/century)	-41.15	-30.1
Derivative of POLE_DEC(deg/century)	-2.01	-0.05

Table A.5: Effect of SARTopo Height estimates on Spin Parameter Fit. The use of the SARTopo heights does not substantially alter the estimates of the spin rate, pole position, or derivative of spin rate. It does alter our estimate of the rate of change of the spin axis orientation, our weakest result.